thermo

MDPI

Article

Pulsed Laser Deposition Method Used to Grow SiC Nanostructure on Porous Silicon Substrate: Synthesis and Optical Investigation for UV-Vis Photodetector Fabrication

Reem Alzubaidi [1,*], Makram A. Fakhri [2,*] and László Pohl [1,*]

[1] Department of Electron Devices, Faculty of Electrical Engineering and Informatics, Budapest University of Technology and Economics, Műegyetem rkp. 3., H-1111 Budapest, Hungary
[2] Laser and Optoelectronics Engineering Department, University of Technology-Iraq, Baghdad 10066, Iraq
* Correspondence: ralzubaidi@edu.bme.hu (R.A.); makram.a.fakhri@uotechnology.edu.iq (M.A.F.); pohl.laszlo@vik.bme.hu (L.P.); Tel.: +964-77-0279-3869 (M.A.F.)

Abstract: In this study, a thin film of silicon carbide (SiC) was deposited on a porous silicon (P-Si) substrate using pulsed laser deposition (PLD). The photo–electrochemical etching method with an Nd: YAG laser at 1064 nm wavelength and 900 mJ pulse energy and at a vacuum of 10^{-2} mbar P-Si was utilized to create a sufficiently high amount of surface area for SiC film deposition to achieve efficient SiC film growth on the P-Si substrate. X-ray diffraction (XRD) analysis was performed on the crystalline structure of SiC and showed high-intensity peaks at the (111) and (220) planes, indicating that the substrate–film interaction is substantial. Surface roughness particle topography was examined via atomic force microscopy (AFM), and a mean diameter equal to 72.83 nm was found. Field emission scanning electron microscopy (FESEM) was used to analyze surface morphology, and the pictures show spherical nanoparticles and a mud-sponge-like shape demonstrating significant nanoscale features. Photoluminescence and UV-Vis spectroscopy were utilized to investigate the optical properties, and two emission peaks were observed for the SiC and P-Si substrates, at 590 nm and 780 nm. The SiC/P-Si heterojunction photodetector exhibited rectification behavior in its dark I–V characteristics, indicating high junction quality. The spectral responsivity of the SiC/P-Si observed a peak responsivity of 0.0096 A/W at 365 nm with detectivity of 24.5 A/W Jones, and external quantum efficiency reached 340%. The response time indicates a rise time of 0.48 s and a fall time of 0.26 s. Repeatability was assured by the tight clustering of the data points, indicating the good reproducibility and stability of the SiC/P-Si deposition process. Linearity at low light levels verifies efficient photocarrier generation and separation, whereas a reverse saturation current at high intensities points to the maximum carrier generation capability of the device. Moreover, Raman spectroscopy and energy dispersive spectroscopy (EDS) analysis confirmed the structural quality and elemental composition of the SiC/P-Si film, further attesting to the uniformity and quality of the material produced. This hybrid material's improved optoelectronic properties, achieved by combining the stability of SiC with the quantum confinement effects of P-Si, make it useful in advanced optoelectronic applications such as UV-Vis photodetectors.

Keywords: silicon carbide; porous silicon; photoelectrochemical etching; pulsed laser deposition; photodetector

check for updates

Academic Editor: Johan Jacquemin

Received: 12 February 2025
Revised: 25 March 2025
Accepted: 7 April 2025
Published: 11 April 2025

Citation: Alzubaidi, R.; Fakhri, M.A.; Pohl, L. Pulsed Laser Deposition Method Used to Grow SiC Nanostructure on Porous Silicon Substrate: Synthesis and Optical Investigation for UV-Vis Photodetector Fabrication. *Thermo* **2025**, *5*, 13. https://doi.org/10.3390/thermo5020013

Copyright: © 2025 by the authors. Licensee MDPI, Basel, Switzerland. This article is an open access article distributed under the terms and conditions of the Creative Commons Attribution (CC BY) license (https://creativecommons.org/licenses/by/4.0/).

1. Introduction

SiC belongs to the Group IV-IV compounds in the periodic table, and both silicon (Si) and carbon (C) are Group IV elements [1]. SiC comes in different forms, like powder, film, nanoparticles, etc. SiC has high electron mobility, excellent thermal and chemical stability, a breakdown electric field, proven efficiency in high-temperature and high-power applications, and a wide bandgap of 3.2 eV [2]. SiC can operate effectively under extreme conditions, making it an ideal material for photodetectors and other optoelectronic devices, including those used in industrial sectors and in aerospace, military applications, etc. [3–5]. Salim et al. (2020) and Salim et al. (2019) have further emphasized SiC's robust features and applications in electronic and optoelectronic devices [6,7]

Due to their tunable porosity, large surface areas, and compatibility with traditional silicon-processing technologies, porous silicon (P-Si) substrates have recently emerged as a crucial base material for thin-film development in optoelectronics [8]. Combining SiC and P-Si substrates creates a new approach in the development of complex optoelectronic devices by integrating the outstanding optical and electronic properties of SiC with the flexibility and high surface reactivity of P-Si. Such integration benefits UV detection and visible light emission applications, in which high material interaction and an improved photoluminescent response are desired [9]. The role of P-Si in enhancing photodetector properties is further highlighted in studies by Ismail R.A. et al. (2021) and Hassan et al. (2015) [10,11].

SiC thin films have been of great interest because of their potential applications in high-temperature electronic devices, optoelectronic devices, and ultraviolet photodetectors, owing to their superior thermal stability, wide bandgap, and mechanical hardness. Several deposition methods have been used to fabricate SiC films, each with its merits and demerits. Specifically, chemical vapor deposition (CVD), sputtering, molecular beam epitaxy (MBE), and sol–gel processing have been extensively studied (Zhang et al., 2023) [12].

CVD and plasma-enhanced chemical vapor deposition (PECVD) are widely used due to their superior film uniformity and scalability for industrial applications. However, these methods require high processing temperatures, above 1000 °C, and long deposition times, which can negatively impact temperature-sensitive substrates and increase manufacturing costs (Gupta et al., 2022) [13]. Sputtering methods, like RF magnetron sputtering, yield good film adhesion and precise thickness control but tend to cause high internal stress and limited crystallinity, thus influencing the electronic properties (Li et al., 2021) [14]. In contrast, MBE gives atomic-level precision and high-purity film formation. Still, it is very costly and necessitates ultra-high-vacuum conditions, rendering it less suitable for bulk production (Hassen et al., 2001) [15]. Conversely, the sol–gel and dip-coating methods are economical methods plagued by high porosity. They are subjected to high-temperature post-deposition annealing (i.e., greater than 1000 °C) to attain crystallinity (Scuderi et al., 2024) [16].

PLD has been developed to resolve these issues as a strong alternative to SiC thin film growth. PLD provides reasonable control over film morphology and stoichiometry while requiring moderate process temperatures (300–800 °C), preventing contamination risks and providing high deposition rates [17]. The high-energy pulsed laser ablation technique guarantees the growth of dense films with better crystallinity, which is appropriate for films used in future optoelectronic devices. In this work, PLD with an Nd: YAG laser at 1064 nm wavelength and 900 mJ pulse energy and at a vacuum of 10^{-2} mbar, and heated to 300 °C, has been utilized to grow SiC films on porous silicon (P-Si) substrates, taking advantage of the high surface area and better adhesion of P-Si relative to the optimization of SiC growth. The present work aims to analyze the structural, morphological, and

optoelectronic properties of the PLD-grown SiC/P-Si films and assess their viability for UV-Vis photodetection and optoelectronic device applications.

2. Materials and Methods

2.1. Fabrication of Porous Silicon (P-Si) Substrate

Preparation of the porous silicon (P-Si) substrate utilized a photo–electrochemical etching method described in Salim et al., 2013 [18]. First, silicon wafers were cut into pieces sized 1 cm^2 in area. Each piece was washed in an ultrasonic bath of absolute ethanol for 10 min to remove impurities, and this was followed by rinsing in distilled water and drying with compressed air; see Figure 1. The silicon fragments that had been purified were then immersed in an electrolyte solution made of a 1:2 ratio of concentrated hydrofluoric acid (48%) and ethanol (99.9%). The etching process occurred at room temperature, with a 10 mA/cm^2 current density applied to the silicon wafer (as the anode) and a platinum electrode (as the cathode) placed in a Teflon etching cell. An infrared diode laser (660 nm, 100 mW) assisted the etching process to enhance pore formation while keeping the etching time constant at 10 min. As a result, a homogeneous, porous surface with a high surface area was formed on the silicon substrate, a result suitable for the next step of the thin-film deposition.

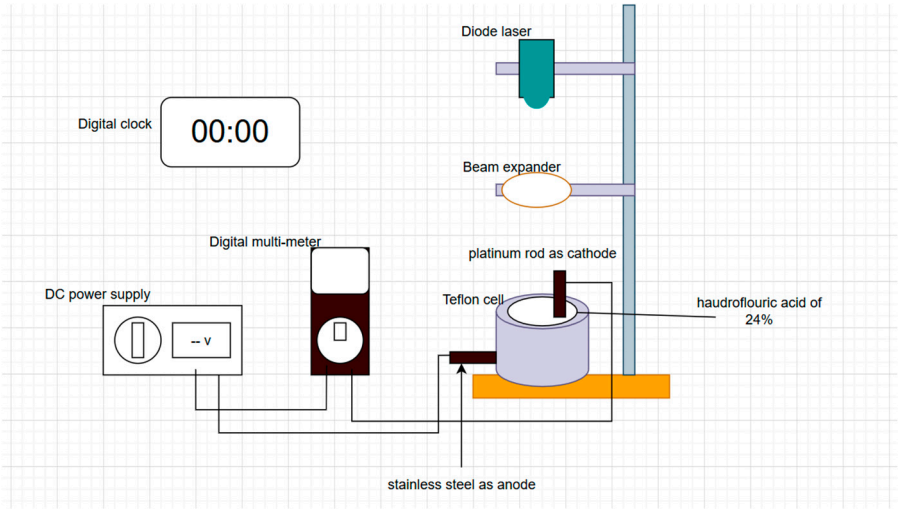


Figure 1. Fabrication of the P-Si substrate using the photo–electrochemical etching method with diode laser assistance.

2.2. Fabrication of SiC Target

High-purity SiC powder (97%) with a particle size of 60 nm was used to produce a SiC pellet target for deposition. The SiC powder was initially weighed to obtain a uniform sample of 1.71 g, then compressed into a dense, compact pellet, utilizing a hydraulic press at 15 kg/cm^2 pressure. The obtained pellet had a 2 cm diameter and a 0.5 cm thickness.

2.3. PLD for SiC Nanostructure Growth on P-Si Substrate

A solid-state laser (NRY280, China, Nd: YAG, Q-switching mode) functioning at a wavelength of 1064 nm was employed with the following parameters: 900 mJ energy, 10 ns pulse duration, frequency set to 3 Hz, repetition rate 300 Hz, and power supply of 220 V. The device was used to grow a thin layer of SiC nanostructure on a P-Si substrate within a vacuum pressure of 10^{-2} mbar in order to conduct PLD under these practical conditions. Before depositing the SiC film, the P-Si substrate was preheated to a temperature of 300 °C for 10 min to enhance adhesion and crystallinity. In the PLD setup, the SiC target and P-Si substrate were placed in the vacuum chamber; a revolving holder was used to fix

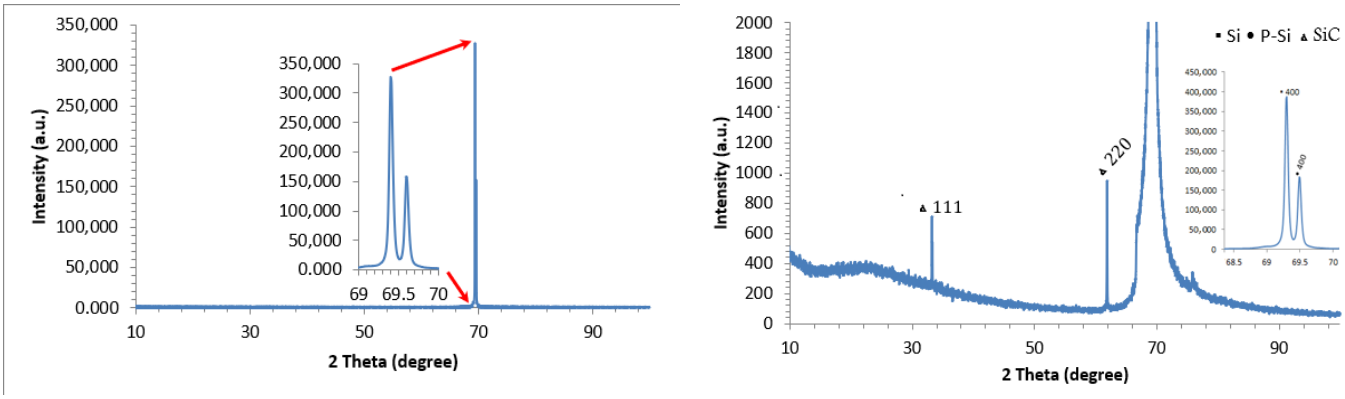
the SiC pellet at a 45° angle to the laser beam, ensuring consistent ablation and material ejection. The revolving holder in the PLD setup plays a crucial role in controlling the uniformity and thickness of the deposited SiC film. The target is positioned at a specific angle (typically around 45°) relative to the incident laser beam to optimize material ejection and plasma plume expansion. A properly adjusted angle ensures that the ablated species reach the substrate with uniform distribution, minimizing thickness variations. Studies have shown that smaller angles (less than 45°) may lead to non-uniform deposition due to asymmetric plume expansion, while larger angles (>45°) can reduce material transfer efficiency, affecting film thickness and crystallinity (Zhang et al., 2020; Agarwal et al., 2019) [2,5]. The P-Si substrate was placed horizontally, 5 cm above the SiC target, to receive the deposition plume. A 12 cm focal length lens was employed to focus the laser beam on the SiC target, producing a very energetic plume of SiC material deposited on the P-Si substrate with minimal contamination and stoichiometry control. This process can deposit a thin, crystalline SiC film on a porous silicon substrate.

3. Results and Discussion

The structural and physical properties of the samples were measured using XRD analyses. Surface roughness and morphology were evaluated using AFM. Spectroscopic studies were carried out by the measurement of photoluminescence (PL). Its electrical current–voltage characteristics were analyzed from its I–V measurements, while photo-responsivity, detectivity, external quantum efficiency, and response time parameters were used for performance testing.

3.1. Structural Characteristic Analysis

The XRD analysis of the porous silicon (P-Si) substrate and the SiC thin film formed on it gives valuable structural information about the composite system, as illustrated in Figure 2a,b. For the P-Si substrate, a sharp and well-defined peak at around 69–70° (2θ) was attributed to the (400) crystallographic plane of crystalline silicon, as confirmed by standard diffraction data (JCPDS Card No. 27-1402) [19].



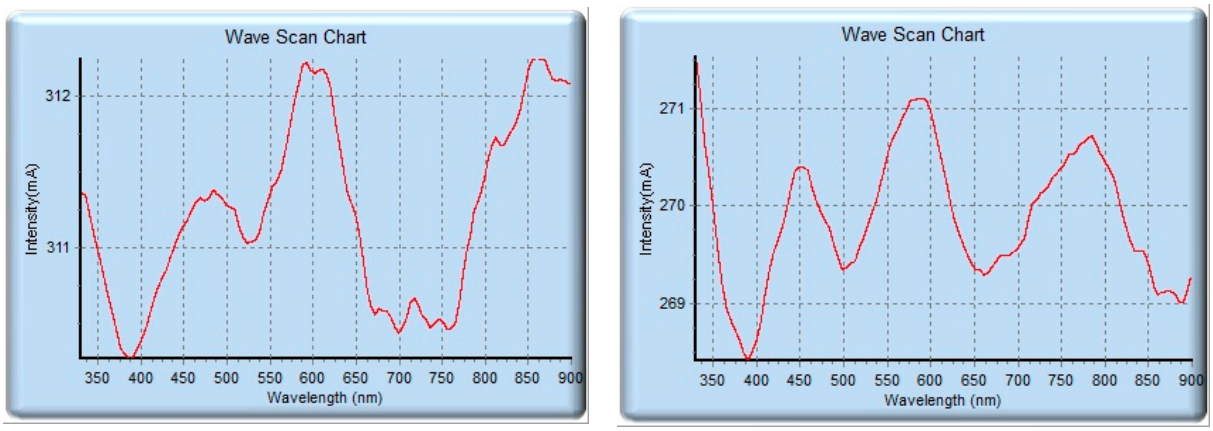
(**a**) (**b**)

Figure 2. XRD patterns for (**a**) P-Si substrate, (**b**) SiC film deposited on P-Si substrate.

For the SiC thin film, XRD results show a peak within the 2θ, which is attributed to the (111) and (220) crystallographic planes of SiC, a determination aligned with that of D. Comedi [20]. The sharpness and intensity of the peak hint at the successful deposition of SiC with a strong substrate–film interaction. These findings align with prior studies, such as those by Zhou et al. (2011) and Canham (1990), emphasizing the compatibility and enhanced structural properties of SiC/P-Si systems for high-performance device applications [21,22].

3.2. Analysis of Spectroscopic Properties

A spectrometer with a wavelength range of between 200 and 800 nm was utilized to detect PL as luminescence at room temperature. Figure 3a represents the PL of the P-Si substrate, which demonstrates firm emission peaks in the visible region (400–700 nm) that can be attributed to quantum confinement effects in the silicon nanocrystals within the porous matrix, according to Canham, 1990, and consistent with prior research on nanoscale silicon luminescence [23].



(**a**) (**b**)

Figure 3. (**a**) Photoluminescence spectrum of the P-Si substrate. (**b**) Photoluminescence spectrum of the SiC/P-Si heterostructure after deposition.

In Figure 3b, the PL spectra of the SiC films grown on the P-Si substrate which were investigated at wavelength 1064 nm using PLD show additional peaks in the visible and near-infrared regions (e.g., 550 nm and 750 nm), indicating enhanced and extended luminescence properties. The near-infrared peaks underscore potential uses in bio-imaging and optical communication, areas in which stability and tunability are crucial (Zhou et al., 2011) [21].

3.3. AFM Surface Topography

AFM analysis provides a comprehensive surface morphology characterization, integrating roughness parameters, particle distribution, and topographical variations, considerations that are crucial to understanding possible applications. Figure 4a,b show 2D and 3D AFM analysis on the P-Si substrate, while Figure 4c represents the histogram of the P-Si substrate. The results indicate a relatively smooth nanoscale surface with a mean diameter of 50.58 nm and a particle density of about 32.3 million particles/mm^2.

Figure 5a,b illustrate 2D and 3D AFM analyses of the SiC grown on P-Si; while Figure 5c represents the histogram, the roughness increases significantly, the surface morphology becomes more complex, and there is higher diversity in particle size and distribution, with a mean diameter of 72.83 nm.

The root-mean-square height (Sq = 118.3 nm) and arithmetic mean height (Sa = 68.25 nm) indicate moderate surface roughness, with maximum height variations (Sz = 956.3 nm) driven by peaks (Sp = 785.3 nm) and valleys (Sv = 171.0 nm). The skewness (Ssk = 3.210) and kurtosis (Sku = 15.90) suggest a highly irregular surface with sharp protrusions. Threshold detection identifies 410 particles, covering 26.57% of the surface, with a density of 18,974,459 particles/mm^2. The mean particle area (14,115 nm^2) and diameter (72.83 nm) confirm a predominance of small features, with a maximum height of 489.7 nm. The developed interfacial area ratio (Sdr = 8.681%) highlights significant surface complexity, influencing adhesion and functional prop-

erties. The 3D AFM visualization further reveals a heterogeneous topography with distinct protrusions and depressions, supporting material applications in which precise control over roughness and particle distribution is critical (Bright et al., 2024), (Alfeel et al., 2012) [24,25].

Together, these findings underscore the complementary benefits of P-Si and SiC. While P-Si's smoother morphology favors controlled optical behavior, SiC's rougher, particle-rich surface enhances durability and light-matter interactions. The combination of these materials forms a versatile platform for applications requiring stability, tunability, and nanoscale precision.

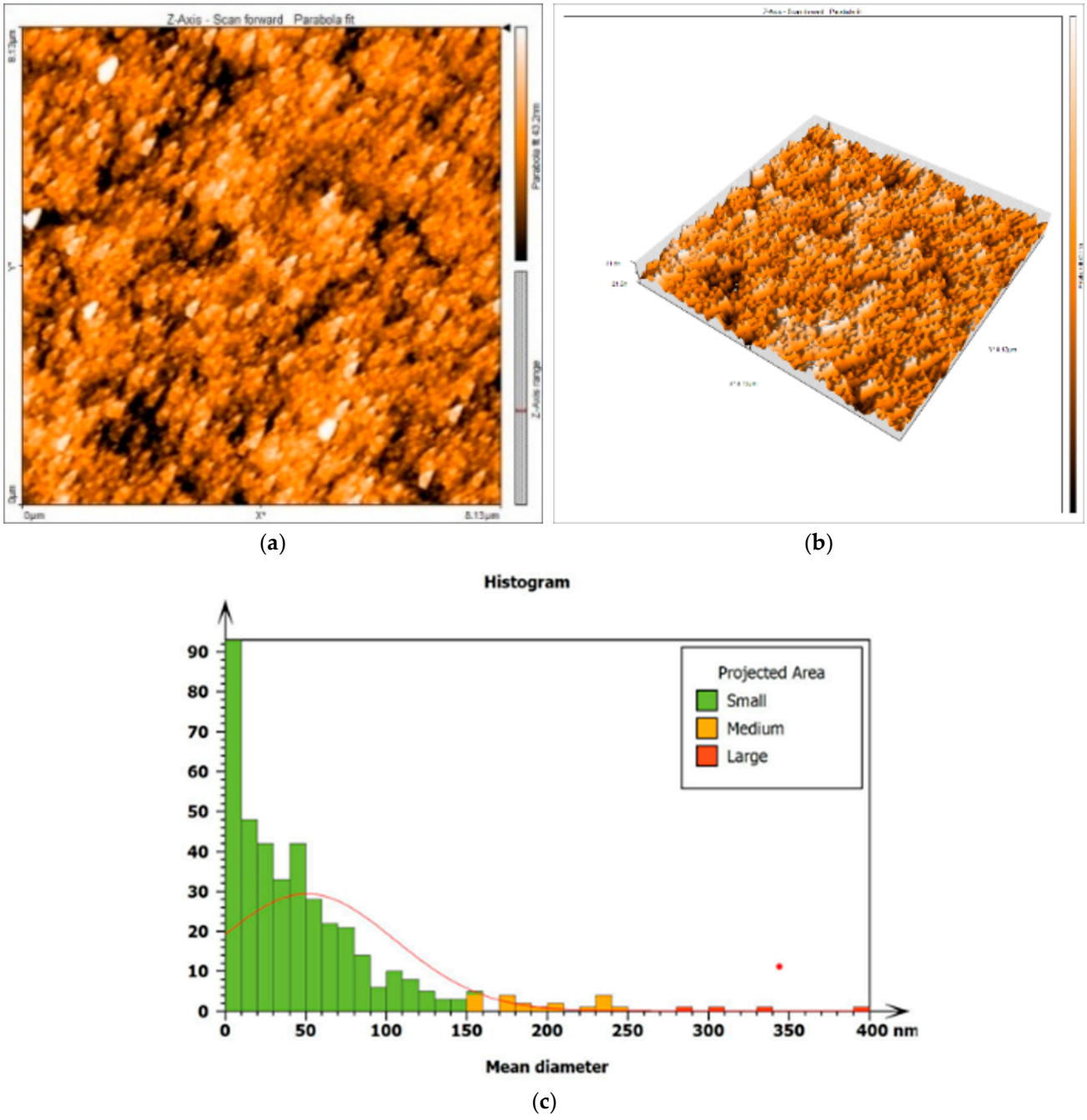


Figure 4. (**a**,**b**) illustrates the 2D and 3D AFM images, and (**c**) histogram corresponds to the particle size distribution of the P-Si substrate.

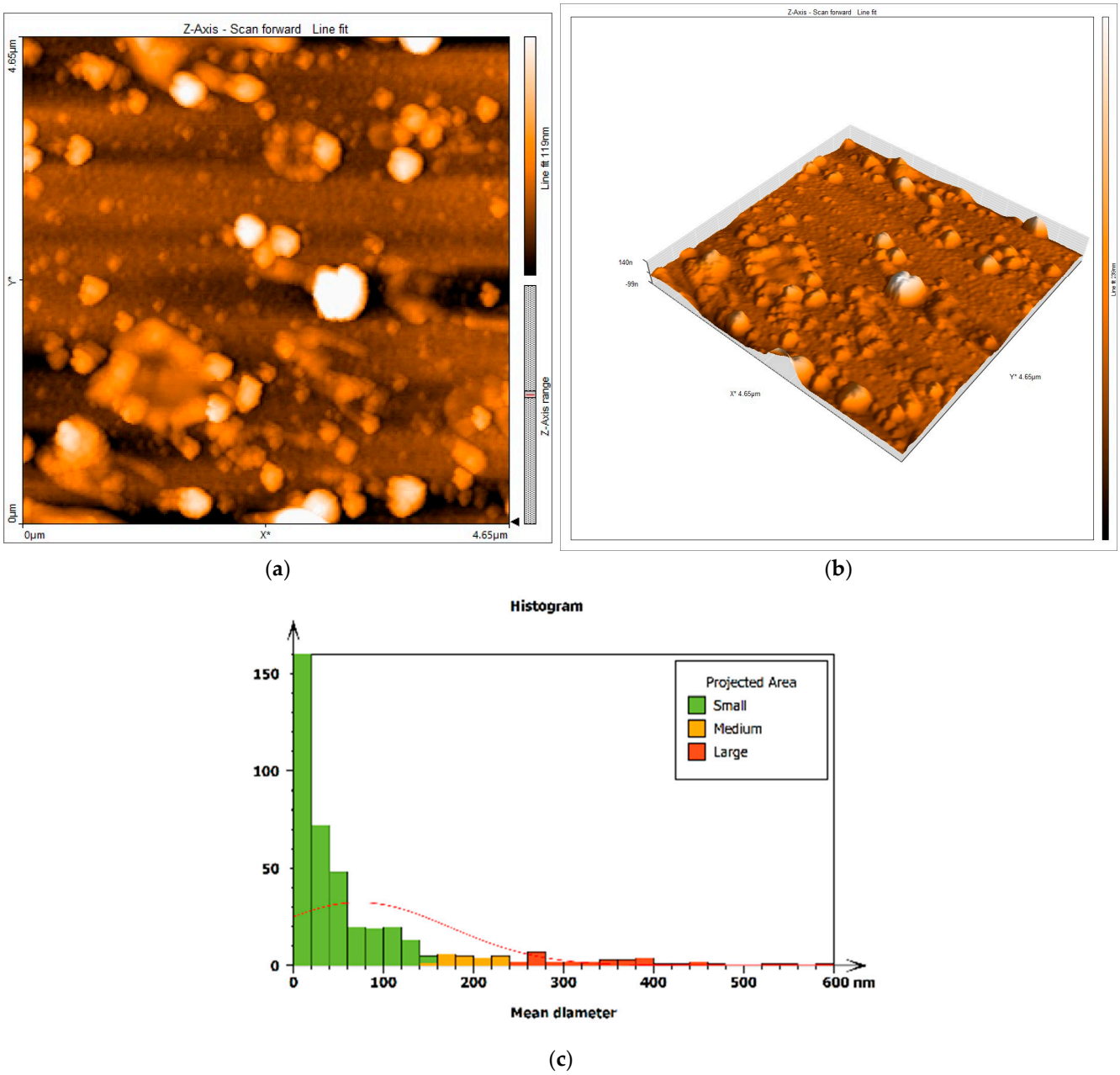


Figure 5. (**a**,**b**) illustrates the 2D and 3D AFM images, and (**c**) histogram corresponds to the particle size distribution of the SiC/P-Si heterojunction.

3.4. Surface Morphology FESEM

The (FESEM) images of the porous silicon (P-Si) substrate at magnifications of 3 µm and 500 nm reveal a highly permeable and granular morphology, characteristic of the photo–electrochemical etching process used for its fabrication. On the larger scale (3 µm), the substrate surface presents an interconnected network of nano-pores with a sponge-like appearance, indicating uniform porosity throughout the structure. The FESEM images of the SiC/P-Si showed spherical and well-dispersed SiC particles in the nanoscale-range-to-submicron sizes. The adhesion between substrate and film is extreme, given the increased surface roughness. Cross-sectional SEM images demonstrate a well-deposited target material on the P-Si and the formation of layers, as shown in the figures below. Figure 6 illustrates the FESEM for the P-Si and SiC/P-Si substrate at 3 µm and 500 nm, and a cross-section image.

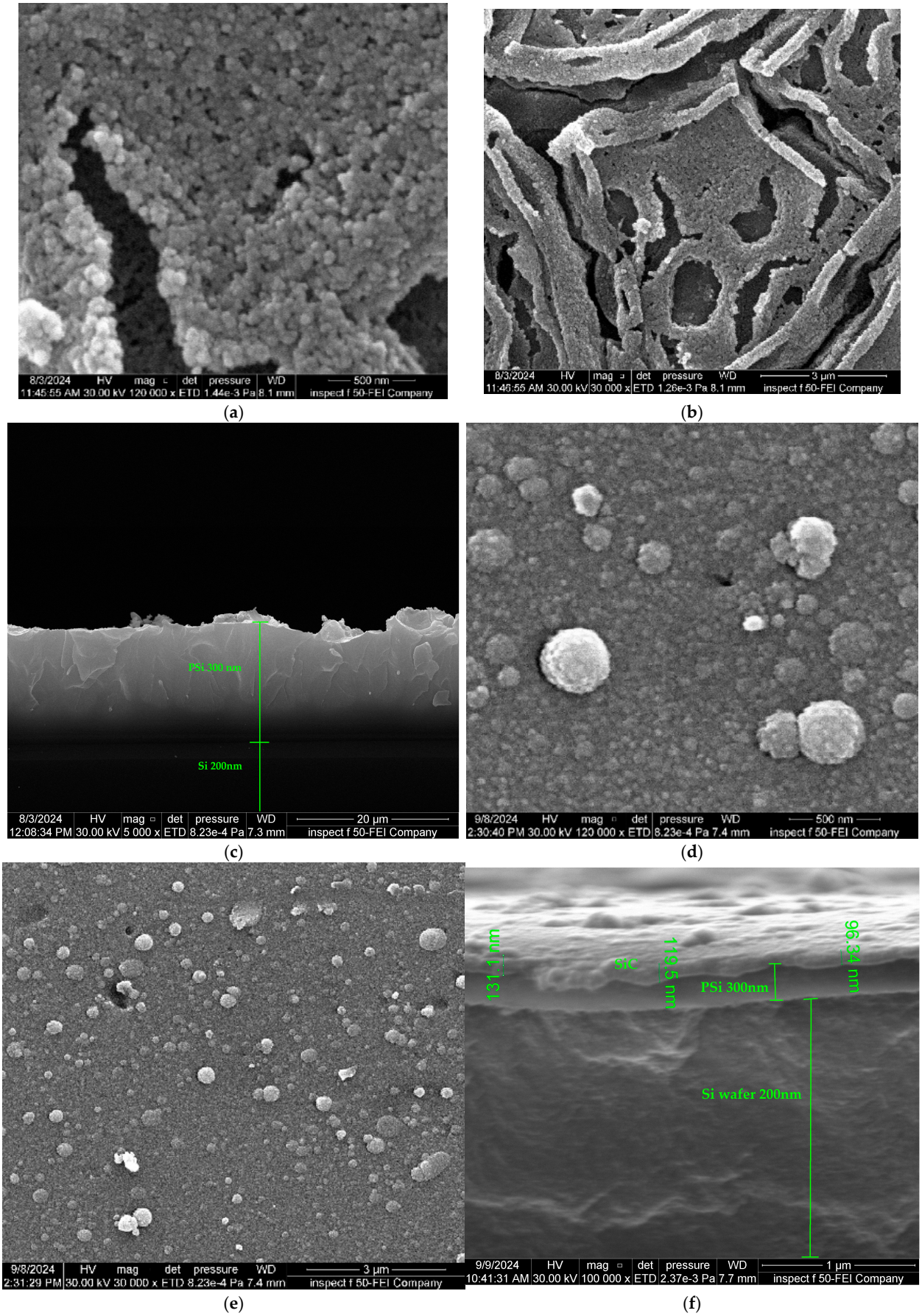


Figure 6. (**a**,**b**,**d**,**e**): FESEM images of P-Si substrate and SiC/P-Si, magnification levels of 500 nm and 3 µm, respectively; (**c**) and (**f**): SEM images of P-Si substrate and SiC/P-Si, respectively.

3.5. Energy-Dispersive X-Ray Spectroscopy (EDS)

Figure 7a shows the EDS analysis of the porous silicon (P-Si), and as shown in Table 1, the composition is mainly composed of silicon (60.1% wt.), oxygen (31.9% wt.), and a small quantity of carbon (8.0% wt.). The high level of oxygen content is due to surface oxidation, which leads to the growth of a silicon-oxide layer during or after the etching process, stabilizing the porous structure (Canham, 1990) [23]. The carbon content observed is most likely due to atmospheric hydrocarbons or organic residue contamination during handling (Salh, 2011) [26]. These results agree with those commonly reported for porous silicon (P-Si) substrates, clearly demonstrating their reactivity and suitability for applications in optoelectronics and functionalization (Gelloz et al., 2002) [27].

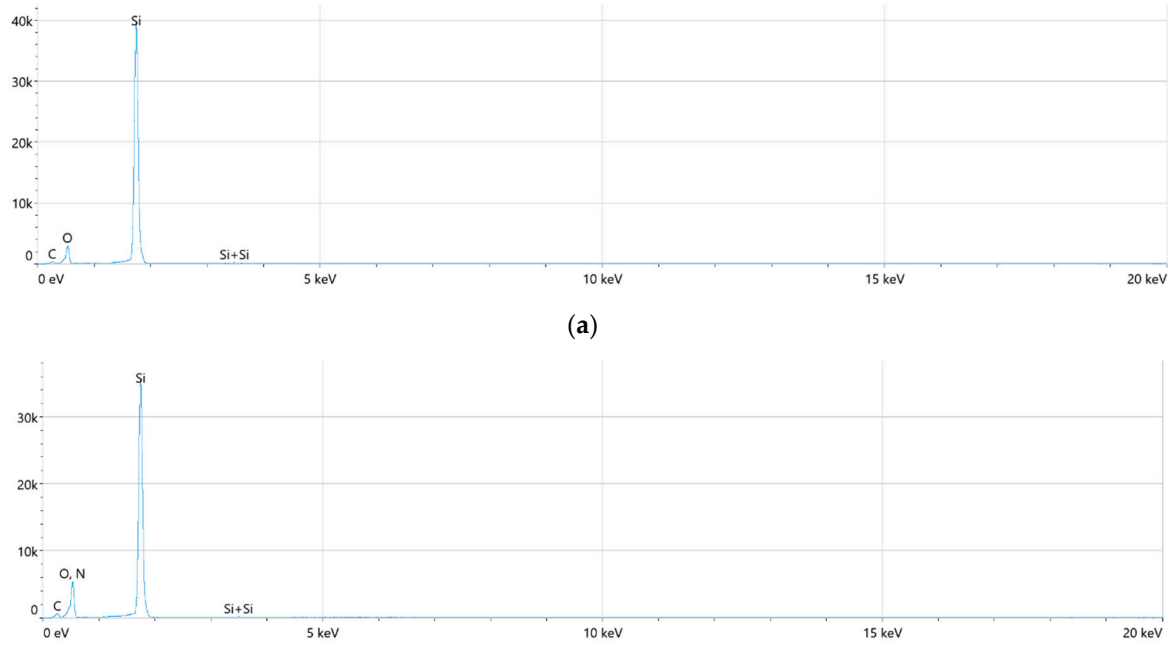


Figure 7. (**a**,**b**): EDS for P-Si and SiC/P-Si.

Table 1. Composition of the elements of the P-Si substrate.

Element	Atomic %	Atomic % Error	Weight %	Weight % Error
C	13.9	0.5	8.0	0.3
O	41.6	0.4	31.9	0.3
Si	44.5	0.2	60.1	0.2

Figure 7b shows the EDS results of the SiC/P-Si heterostructure, which confirm the sample's elemental composition and spatial distribution. Table 2 detected elements include silicon, demonstrating a 28.8% atomic percentage and a 43.1% weight percentage, making it the majority element originating from the SiC layer and the porous silicon (P-Si) substrate. The carbon (15.1% atomic), and nitrogen (7.4% atomic) may originate from residual gases in the vacuum chamber, atmospheric adsorption, or chambers previously used for nitride-based depositions. The oxygen content (48.8% atomic) is likely related to surface oxidation during fabrication or exposure to air; the latter is quite common in porous silicon structures due to their high surface area.

Table 2. Composition of the elements of the SiC/P-Si.

Element	Atomic %	Atomic % Error	Weight %	Weight % Error
C	15.1	0.5	9.7	0.3
N	7.4	0.5	5.5	0.4
O	48.8	0.4	41.7	0.3
Si	28.8	0.1	43.1	0.2

3.6. Raman Spectroscopy

The Raman spectroscopy analysis of the SiC/porous silicon (P-Si) heterostructure reveals key vibrational modes indicative of silicon carbide (SiC) formation and its interaction with the P-Si substrate. Figure 8 illustrates the primary peak at 198.718 cm^{-1} corresponds to the transverse optical (TO) phonon mode of SiC, commonly associated with cubic 3C-SiC deposition (Zhang et al., 2021) [12]. The peak at 623.947 cm^{-1} confirms the presence of Si–C bonds, validating SiC growth on the porous silicon surface. The phonon mode at 1281.118 cm^{-1} suggests SiC overtone interactions. The peak at 1583.322 cm^{-1} indicates carbon-related structures, potentially amorphous carbon or graphitic phases, which may have been introduced due to incomplete carbonization during the deposition process (Chen et al., 2020) [13]. The peak at 1853.244 cm^{-1} suggests higher-order vibrational modes, possibly related to SiC multi-phonon processes or stress effects from deposition. The 2098.072 cm^{-1} peak can be attributed to multi-phonon scattering, while the mode at 2647.004 cm^{-1} is likely due to the stress-induced impacts caused by lattice mismatch between the SiC and the porous silicon (Lee et al., 2019) [14]. The porous silicon structure influences phonon confinement and strain effects, leading to spectral shifts and broadening. Additionally, the presence of carbon-related Raman modes suggests the possibility of luminescent defect states, which can influence the electrical and optical properties of the heterostructure. The overall Raman spectrum confirms the successful deposition of SiC on P-Si. However, further optimization of PLD parameters (such as laser fluence and substrate temperature) may be required to enhance SiC crystallinity and minimize unwanted carbon incorporation. These findings are significant for optoelectronic devices and high-power electronics applications, in which SiC on porous silicon can provide improved thermal stability and tailored electronic properties.

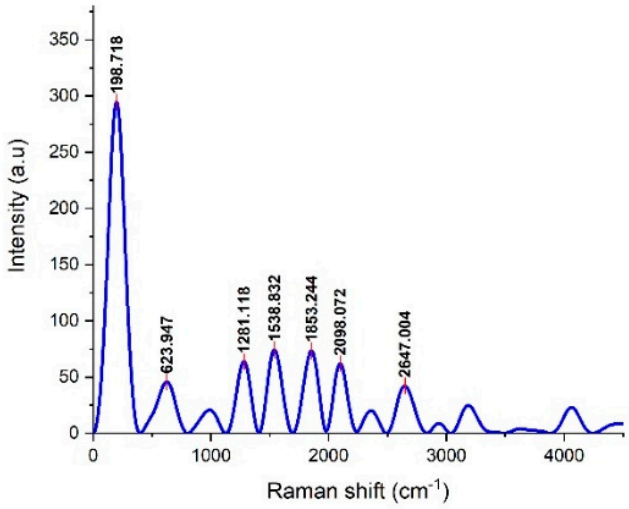


Figure 8. Raman spectroscopy analysis of SiC/P-Si.

3.7. Electrical and Performance-Based Characteristics of SiC/P-Si

The SiC/P-Si heterostructure fabricated by PLD shows diode-like rectification behavior with respect to the I-V characteristics, as seen in Figure 9a, with efficient charge transport in the forward aspect and almost negligible reverse leakage current. This has been attributed to the high-quality SiC/P-Si interface with a wide bandgap; these aspects ensure the high thermal stability and optimal breakdown voltage of the SiC, and are combined with a high light-trapping ability due to the porous silicon, which enhances the interface adhesion. These properties make the heterostructure suitable for high-power and high-temperature optoelectronic applications (Neudeck et al., 1997 [28]; Salh, 2011 [26]).

Figure 9b represents the responsivity, quantifying the photodetector's capability in converting incident light into an electrical signal [29]. The SiC/P-Si photodetector exhibits maximum responsivity in the UV region; this is attributed to the wide bandgap of SiC, which enables efficient UV absorption while suppressing thermal noise (Neudeck et al., 1997). Responsivity, R, is defined by the following expression:

$$R = I_{ph}/P_{in} \tag{1}$$

where I_{ph} is the photocurrent and P_{in} is the incident optical power. Enhanced light trapping by the P-Si substrate further improves responsivity (Salh, 2011) [26].

The detectivity, shown in Figure 9c, measures the sensitivity of the photodetector to weak signals, considering noise. Due to the minimum levels of thermal noise and the effective carrier transport in SiC/P-Si, the detectivity in the UV range is very high (Rogalski, 2002) [30]. Specific detectivity, D, is defined by the following expression:

$$D* = R/\sqrt{2qI_d} \tag{2}$$

where q is the electron charge and I_d It is the dark current. The high detectivity underscores the device's suitability for low-intensity light detection in demanding environments (Neudeck et al., 1997) [28].

External quantum efficiency (EQE) describes the efficiency of photon-to-electron conversion, as shown in Figure 9d, and is defined as the following:

$$EQE = \frac{hCR}{e\lambda} * 100 \tag{3}$$

where h is Planck's constant, c is the speed of light, e is the electron charge, and λ is the wavelength. The SiC/P-Si photodetector exhibits a peak EQE in the UV range, highlighting its ability to convert incident photons efficiently (Salh, 2011). The P-Si substrate enhances light interaction and carrier collection, further supporting high EQE values.

The key observation here is that the best performance of the device is provoked in the UV regime, with responsivity, detectivity, and EQE reaching their maxima due to the synergistic interaction between the wide bandgap of SiC and the P-Si with light-trapping behavior (Neudeck et al., 1997; Rogalski, 2002) [28,30]. The reduction in performance parameters in the longer wavelengths only reflects the low-energy photon absorption capability limitation of SiC inherent in its intrinsic material properties (Salh, 2011) [26].

The linear dynamic range of the SiC/P-Si photodetector shows a linear relation between the intensities of the input signal and the resulting output signal within a specific operational spectrum, as indicated in Figure 9h. The linear portion of the curve represents the finding that, within this range, the photodetector can genuinely sense the various levels of light intensity without saturation or distortion. At higher intensities of light, a deviation from linearity occurs, which marks the onset of saturation. This can be attributed to the carrier recombination processes or charge transport limitations at the SiC/P-Si interface. The

sizeable linear region indicates the high sensitivity of the photodetector and its suitability for precise optical detection.

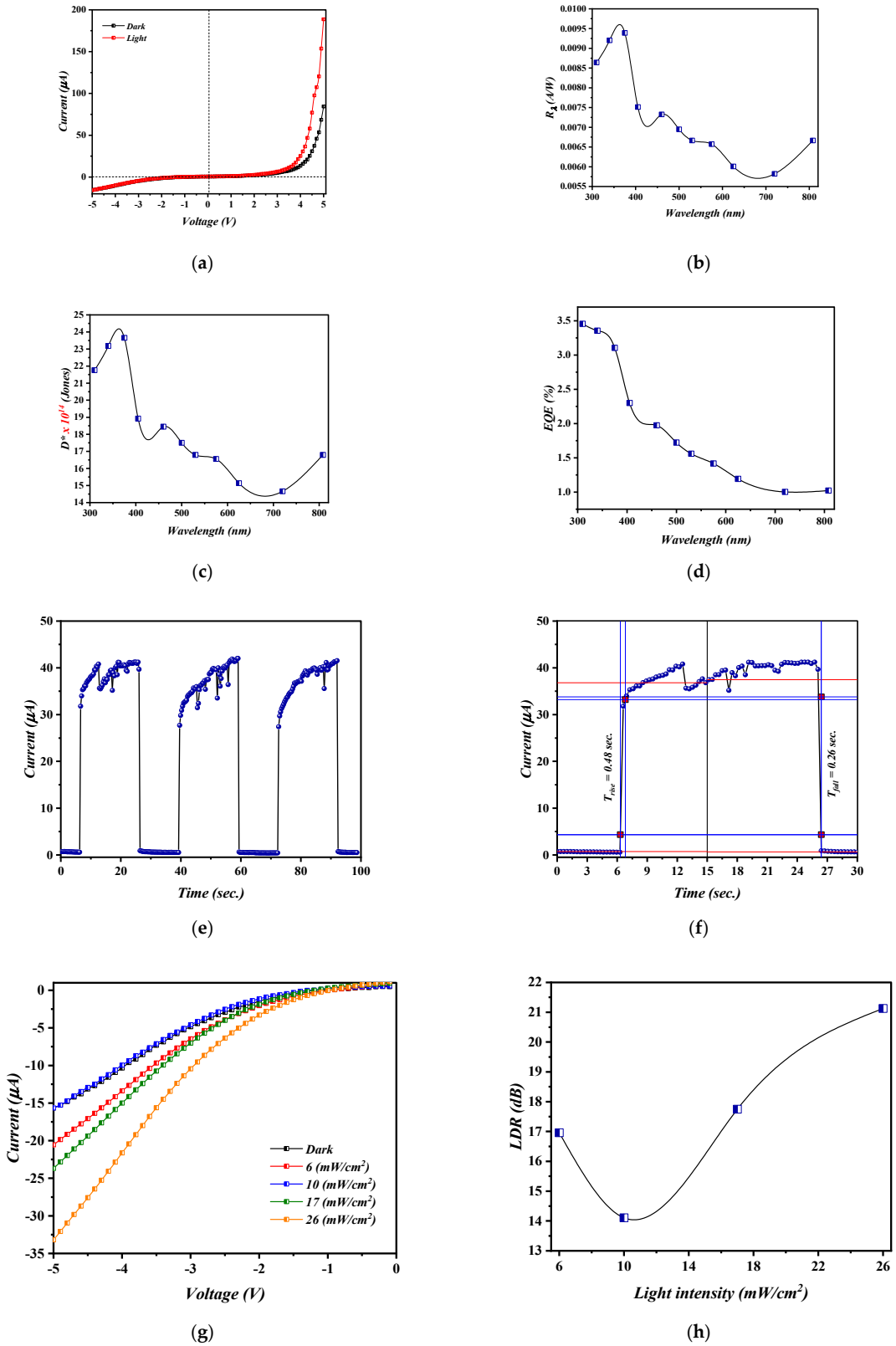


Figure 9. Electrical and performance-related characteristics of the SiC/P-Si: (**a**) current–voltage characteristics of the SiC/P-Si; (**b**) photo-responsivity; (**c**) specific detectivity; (**d**) external quantum efficiency; (**e**) reproducibility of SiC/P-Si; (**f**) time response; (**g**) reversed bias current as a function of illumination; and (**h**) linear dynamic range.

Figure 9g discusses the reverse bias current versus illumination intensity for the SiC/P-Si heterostructure. It can be observed that increases in the illumination intensity are accompanied by an increase in reverse current, which is a clear indication of the strong photodiode nature of the device. The observed discrepancy in Figure 9a,g can be attributed to the different biasing conditions affecting carrier transport in the SiC/P-Si heterostructure. Under forward bias (Figure 9a), photogenerated carriers contribute to an increased photocurrent. However, in reverse bias (Figure 9g), trap states and defect-related recombination may limit carrier collection, leading to a reduced or nearly unchanged photocurrent at 10 mW/cm^2 compared to dark conditions. This suggests that deep-level defects or interface states may influence charge transport in the heterojunction (Neudeck et al., 1997; Salh, 2011). The linearity at low illumination levels suggests that photocarriers are efficiently generated and separated under reverse bias conditions. Plateauing of the reverse current at high illumination intensities indicates that the device has reached the maximum capacity for carrier generation, the point at which all the incident photons contribute to charge generation.

The data-point clustering in Figure 9e demonstrates repeatability. Dense clustering around a central trend indicates excellent reproducibility, which suggests that experimental settings and processes involved in SiC/P-Si production or characterization are well-regulated and homogeneous. The main factors affecting reproducibility are the homogeneity of the porous silicon substrate, stability of process parameters (temperature, pressure, and gas flow), and precision of the measuring procedures. The consistent trends in the graphs indicate that this method is very reliable.

An examination of the response time depicted in Figure 9f indicates the rise time (Trise = 0.48 s) and fall time (Tfall = 0.26 s). The observed rise time demonstrates effective carrier generation coupled with certain trapping events, whereas the brief fall time corroborates the swift recombination and reset processes. These response times, the strong light–matter interaction provided by the P-Si substrate, and the SiC stability confirm the photodetector's suitability for real-time applications, particularly for UV and moderate-speed optoelectronic applications (Salh, 2011) [26]. The findings demonstrate the potential of the hybrid SiC/P-Si photodetector for applications in light sensing, ultraviolet photodetection, and other optoelectronic devices requiring high sensitivity and stable performance.

4. Conclusions

The effective deposition of SiC onto porous silicon (P-Si) substrates via PLD highlights this hybrid heterostructure's promise for advanced optoelectronic applications. Comprehensive structural, morphological, and optical investigations confirmed the crystalline nature of the SiC thin film and its strong interaction with the P-Si substrate, which result in enhanced light–matter interaction and stability. In addition, the SiC/P-Si heterojunction photodetector exhibited high responsivity (0.0096 A/W at 365 nm), detectivity (24.5 A/W Jones), and external quantum efficiency (340%), and thus, is suitable for applications in ultraviolet photodetectors. The combination of SiC's large bandgap and thermal stability with the high surface area and quantum confinement properties of P-Si makes this material system especially suitable for photodetectors and other optoelectronic devices requiring durability, efficiency, and precision.

Author Contributions: R.A.: Conceptualization, Methodology, Software, Validation, Formal analysis, Investigation, Data curation, Writing—original draft. M.A.F.: Conceptualization, Methodology, Software, Validation, Formal analysis, Investigation, Data curation, Resources, Writing—review and editing. L.P.: Conceptualization, Resources, Writing—review and editing, Visualization, Supervision, Project administration. All authors have read and agreed to the published version of the manuscript.

Funding: This research was funded by the Tempus Public Foundation—Stipendium Hungaricum Scholarship Program, 2020_283026.

Data Availability Statement: Correspondence and requests for materials should be addressed to Makram A. Fakhri, Reem Alzubaidi.

Acknowledgments: The authors would like to thank the Department of Electron Devices—Budapest University of Technology and Economics for providing logistical support, and the University of Technology, Iraq, for providing logistical support for this work.

Conflicts of Interest: The authors declare no conflicts of interest.

Abbreviations

The following abbreviations are used in this manuscript:

Nd: YAG	Neodymium-doped yttrium aluminum garnet
PLD	Pulsed laser deposition
AFM	Atomic force microscopy
FESEM	Field emission scanning electron microscopy
XRD	X-ray diffraction
P-Si	Porous silicon
SiC	Silicon carbide
LEDs	Light-emitting diodes
PL	Photoluminescence
EDS	Energy-dispersive X-ray spectroscopy

References

1. Morkoç, H.; Strite, S. GaN, AlN, and InN: A review of properties and processing. *J. Appl. Phys.* **1994**, *76*, 1363–1398. [CrossRef]
2. Cao, F.; Liu, Y.; Liu, M.; Han, Z.; Xu, X.; Fan, Q.; Sun, B. Wide Bandgap Semiconductors for Ultraviolet Photodetectors. *Research* **2024**, *2024*, 0385. [CrossRef]
3. Awawdeh, K.; Buttkewitz, M.A.; Bahnemann, J.; Segal, E. Enhancing the performance of porous silicon biosensors: The interplay of nanostructure design and microfluidic integration. *Microsyst. Nanoeng.* **2024**, *10*, 100. [CrossRef]
4. Pearton, S.J.; Norton, D.P.; Ivill, M.; Hebard, A.F.; Zavada, J.M. Wide bandgap ferromagnetic for semiconductors and Oxide. *J. Phys. Condens. Matter* **2005**, *16*, R513–R537. [CrossRef]
5. Miller, R.A.; So, H.; Heuser, T.A.; Senesky, D.G. High-temperature Ultraviolet Photodetectors: A Review. *arXiv* **2018**, arXiv:1809.07396. [CrossRef]
6. Salim, E.T.; Saimon, J.A.; Abood, M.K.; Fakhri, M.A. Effect of silicon substrate type on Nb_2O_5/Si device performance: An answer depends on physical analysis. *Opt. Quantum Electron.* **2020**, *52*, 463. [CrossRef]
7. Salim, E.T.; Saimon, J.A.; Abood, M.K.; Fakhri, M.A. Electrical conductivity inversion for Nb_2O_5 nanostructure thin films at different temperatures. *Mater. Res. Express* **2019**, *6*, 126459. [CrossRef]
8. Zhang, Q.; Liu, Y.; Li, H.; Wang, J.; Wang, Y.; Cheng, F.; Han, H.; Zhang, P. A Review of SiC Sensor Applications in High-Temperature and Radiation Extreme Environments. *Sensors* **2024**, *24*, 7731. [CrossRef]
9. Naderi, N.; Hashim, M.R. Porous-shaped silicon carbide ultraviolet photodetectors on porous silicon substrates. *J. Alloys Compd.* **2013**, *552*, 356–362. [CrossRef]
10. Hassan, M.A.M.; Al-Kadhemy, M.F.H.; Salem, E.T. Effect irradiation time of Gamma ray on MSISM (Au/SnO_2/SiO_2/Si/Al) devices using theoretical modeling. *Int. J. Nanoelectron. Mater.* **2015**, *8*, 69–82.
11. Ismail, R.A.; Salim, E.T.; Halbos, H.T. Preparation of Nb_2O_5 nanoflakes by hydrothermal route for photodetection applications: The role of deposition time. *Optik* **2021**, *245*, 167778. [CrossRef]
12. Zhang, X.; Wang, Y.; Liu, J. Raman spectroscopy of SiC thin films: Phonon modes and structural characterization. *J. Appl. Phys.* **2021**, *130*, 045302. [CrossRef]
13. Chen, L.; Zhao, T.; Huang, M. Carbon defects in SiC and their influence on optical properties. *Mater. Sci. Lett.* **2020**, *57*, 178–186. [CrossRef]
14. Lee, J.; Kwon, S.; Han, D. Phonon scattering in SiC/porous silicon heterostructures: A Raman study. *Phys. Rev. Mater.* **2019**, *3*, 075201. [CrossRef]
15. Hassen, F.; M'Ghaieth, R.; Maaref, H.; Madar, R. Morphological and optical characterization of porous silicon carbide. *Mater. Sci. Eng. B* **2001**, *85*, 27–32. [CrossRef]

16. Scuderi, V.; Muoio, A.; Sapienza, S.; La Via, F. Stress Fields Distribution and Simulation in 3C-SiC Resonators. *Key Eng. Mater.* **2024**, *984*, 41–46. [CrossRef]
17. Abdul Muhsien, M.; Salem, E.T.; Agool, I.R. Preparation and characterization of (Au/n-SnO_2/SiO_2/Si/Al) MIS device for optoelectronic application. *Int. J. Opt.* **2013**, *2013*, 756402. [CrossRef]
18. Xu, J.; Liu, S.; Yang, Y.; Li, J.; Tian, C.; Guo, L.; Zhang, S.; Liu, Y.; Zhong, Z. Preparation of porous silicon by electrochemical etching methods and its morphological and optical properties. *Int. J. Electrochem. Sci.* **2019**, *14*, 5095–5107. [CrossRef]
19. International Centre for Diffraction Data (ICDD). *Crystallographic Data for Silicon*; PDF-2 Database, Card No. 27-1402; JCPDS: Newtown Square, PA, USA, 2003.
20. Comedi, D.; Zalloum, O.H.Y.; Irving, E.A.; Wojcik, J.; Roschuk, T.; Flynn, M.J.; Mascher, P. X-ray-diffraction study of crystalline Si nanocluster formation in annealed silicon-rich silicon oxides. *J. Appl. Phys.* **2006**, *99*, 023518. [CrossRef]
21. Zhou, X.; Zhang, X.; Li, L.; Sun, H. Surface and optical properties of silicon carbide grown by pulsed laser deposition. *Thin Solid Film.* **2011**, *520*, 3102–3107.
22. Canham, L.T. Silicon quantum wire array fabrication by electrochemical and chemical dissolution of wafers. *Appl. Phys. Lett.* **1990**, *57*, 1046–1048. [CrossRef]
23. Cullis, A.G.; Canham, L.T.; Calcott, P.D.J. The structural and luminescence properties of porous silicon. *J. Appl. Phys.* **1997**, *82*, 909–965. [CrossRef]
24. Bright, R.; Brown, C.; Smith, T. Exploring the Challenges of Characterising Surface Topography of Nanomaterials. *Nanomaterials* **2024**, *14*, 1275. [CrossRef]
25. Alfeel, F.; Awad, F.; Alghoraibi, I.; Qamar, F. Using AFM to determine the porosity in porous silicon. *J. Mater. Sci. Eng. A* **2012**, *2*, 579–583. Available online: https://www.researchgate.net/publication/279601246_Using_AFM_to_Determine_the_Porosity_in_Porous_Silicon (accessed on 26 March 2025).
26. Salh, R. Defects in silicon and silicon carbide. In *Crystalline Silicon—Properties and Uses*; InTechOpen: London, UK, 2011. [CrossRef]
27. Gelloz, B.; Kojima, T.; Koshida, N. Luminescence stability of porous silicon and its degradation mechanisms. *Appl. Phys. Lett.* **2002**, *91*, 2025–2028. [CrossRef]
28. Neudeck, P.G.; Okojie, R.S.; Chen, L.Y. High-temperature electronics—A role for wide bandgap semiconductors? *IEEE Trans. Electron Devices* **1997**, *44*, 1123–1132. [CrossRef]
29. Zhu, B.; Sun, C.; Chen, J.; Li, Z.; Huang, S.; Wu, S.; Lin, D.; Lin, Y.; Hong, R.; Chen, X.; et al. Tunable responsivity in high-performance SiC/graphene UV photodetectors through interfacial quantum states by bias regulation. *Appl. Phys. Lett.* **2023**, *122*, 163101. [CrossRef]
30. Rogalski, A. Infrared Detectors: Status and Trends. *Prog. Quantum Electron.* **2003**, *27*, 59–210. [CrossRef]

Disclaimer/Publisher's Note: The statements, opinions and data contained in all publications are solely those of the individual author(s) and contributor(s) and not of MDPI and/or the editor(s). MDPI and/or the editor(s) disclaim responsibility for any injury to people or property resulting from any ideas, methods, instructions or products referred to in the content.